Tenth USA/Europe Air Traffic Management Research and Development Seminar (ATM2013)

Climate cost functions as a basis for climate optimized flight trajectories

Christine Frömming, Volker Grewe, Patrick Jöckel, Sabine Brinkop, Simone Dietmüller, Hella Garny, Michael Ponater, Eleni Tsati, Sigrun Matthes

Institute of Atmospheric Physics
DLR-German Aerospace Center
Oberpfaffenhofen, Germany

***Abstract*— Climate cost functions are a measure for the climate impact of individual aviation emissions in dependency of the emission location, altitude, time and weather situation during emission. To determine the climate change contribution due to an individual emission as function of emission location, altitude and time, four-dimensional climate cost functions are computed. Therefore the ECHAM5/MESSy Atmospheric Chemistry model (EMAC) has been employed. The emitted trace species are transported by means of the Lagrangian advection scheme ATTILA. To evaluate the climate impact from several emission locations and dates within one simulation, a new submodel (AIRTRAC) has been developed. Chemical changes of ozone, methane and water vapor, as well as contrail formation and aging caused by a particular emission are computed directly on air parcels. For each emission location and date, the changes of radiatively active species and the corresponding radiative forcings are computed, from which the climate cost functions are derived. The climate cost functions form the basis for the optimization of air traffic flight trajectories with respect to minimum climate impact. Typical weather situations are considered and differences in climate impact are investigated. The North Atlantic flight corridor is considered for route optimization.**

Keywords – aircraft emissions, climate impact mitigation, trajectory optimization

I. INTRODUCTION

Aviation contributes about 3-5 % to the total anthropogenic climate impact in terms of radiative forcing. Because of high growth rates of about 5 % per year, the percentage contribution of aviation to climate change is likely to increase in the future. Measures to reduce the climate impact of aviation are necessary. Different approaches for mitigation are conceivable, such as alternative fuels, novel engine concepts, modification of aircraft design, or alternative routing, etc.

The climate impact of non-CO_2 aviation emissions is highly dependent on atmospheric background conditions. Hence the aviation-induced cloudiness and chemical perturbations vary significantly with geographic location, altitude, and time of the emission. If such knowledge about altitude and location dependencies of non-CO_2 aviation effects was considered in the route-planning process, the overall aviation net climate impact could potentially be reduced.

Previous studies, [e.g., 1, 2, 3, 4, 5, 6, 7] examined the altitudinal dependency of contrails, aviation H_2O and NO_x effects, and identified characteristic sensitivities to emission altitudes and tradeoffs between warming and cooling contributions and between short-term and long-term effects. Studies which investigated contrail mitigation [1, 3, 8, 9] found a substantial contrail avoidance potential and evidence of regionally and seasonally compensating effects. Furthermore strong dependency to actual meteorological conditions was identified. A dependency of aviation-induced water vapor perturbation on the flight altitude was found [10, 13, 11], as higher flight altitudes lead to a larger fraction of water vapor emitted in the stratosphere, where water vapor emissions accumulate to larger concentration changes due to the lack of major loss processes. Aviation-induced ozone and methane perturbations resulting from aviation NO_x emissions are also highly dependent on the emission altitude. For a climatological mean situation, air traffic-induced ozone perturbations increase for higher cruise altitudes and decrease for lower cruise altitudes [2, 4, 5, 13]. The reduced ozone impact for lower flight altitudes is mainly caused by faster removal of ozone precursor species at lower flight levels, whereas atmospheric residence times of ozone precursors are longer at higher altitudes, resulting in a more efficient accumulation. A stronger reduction of CH_4 lifetimes was found for lower flight altitudes [12, 13], whereas higher flight altitudes tend to induce a smaller reduction of methane lifetimes. Grewe and Stenke [14] and Fichter [15] found maximum reduction of CH_4 lifetime for emissions in the stratosphere and in the tropical mid-troposphere. Minimum impact was found at tropopause levels, where OH formation is limited because of low water vapor concentration and UV radiation. Most studies investigated the climatological mean situation, whereas in the present study, we concentrate on emission effects for individual days and weather patterns.

The above mentioned results propose a considerable potential for mitigating non-CO_2 air traffic climate impacts by adjusting flight trajectories, which avoid regions and altitudes where emissions cause relatively higher climate impact and prefer regions and altitudes where emissions cause relatively

smaller climate impact. However, most effects were shown to have a strong interconnection to the actual weather situation, related to different transport pathways, different background chemistry, different tropopause height, and the actual occurrence of ice supersaturated regions. Thus for a more sophisticated approach actual meteorological conditions should be considered.

II. Calculation of Climate Cost Functions

Within this paper, a new modeling approach is presented, which provides climate cost functions for a defined weather situation, for the most important aviation emissions, as functions of location, altitude, and time. The climate cost functions are calculated for typical weather patterns over the North Atlantic region, which were derived from a detailed analysis of ERA-interim data including a classification of weather patterns [16]. For each weather pattern a representative day is selected, for which climate cost functions are determined. Since the weather situation changes during the day, the regions are temporally resolved. We refer to this as "time-regions". The ECHAM5/MESSy Atmospheric Chemistry Model (EMAC) [17] is employed for this study, including two essential submodels: ATTILA, a Lagrangian transport scheme [18], and AIRTRAC, calculating the climate impact of aviation emissions as function of the emission location, altitude and time. The calculation of climate cost functions includes the calculation of emission-induced atmospheric changes such as perturbations of nitrogen oxides, ozone, methane, water vapor and the formation of contrails and their optical properties. The instantaneous radiative forcing is calculated online in the model, whereas the adjusted radiative forcing is parameterized based on an analysis of idealized simulations, investigating pulse and sustained emissions. The AIRTRAC submodel has been developed within the EU FP7 project REACT4C (http://www.react4c.eu) and will be employed and further developed within a cooperative project with NASA and DLR.

A. *Lagrangian Approach*

The calculation of climate cost functions requires a separate calculation for every time-region. Hence, the resolution of the climate cost function in time and space defines the number of climate cost function calculations. We denote the number of time-regions with NTR and the individual time-regions with R_i (i=1, …., NTR).

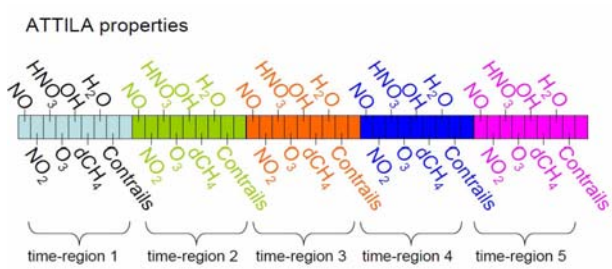

Figure 1. Time-region properties in ATTILA.

We have chosen a Lagrangian approach, since it allows including a multitude of cost function calculations in a single EMAC simulation. Each trajectory or air parcel follows the atmospheric motion and is characterized by its three-dimensional position at every model time step and has an arbitrary number of properties P. For each time-region R_i a set of n properties is assigned. Properties for 5 time-regions are shown exemplarily in Fig. 1, i.e. the contribution of the emissions to the perturbations of NO, NO_2, HNO_3, O_3, CH_4, and H_2O and contrail coverage.

Our modeling approach is based on a detailed modeling of the background processes within EMAC and an additional calculation of the contributions from the emissions released in the respective time-regions. Information from the background processes is transferred to the Lagrangian trajectories and the contributions are calculated based on the results from the detailed process modeling within EMAC. The calculated contributions from the emissions released in the time-regions do not feedback to the base model processes, ensuring identical background meteorology and chemistry for all time-region simulations (Fig. 2).

For every time-region, 50 randomly distributed Lagrangian trajectories are released at the time of emission, to which the emission is equally distributed. This ensures a statistically stable distribution of emissions. In addition ~170 000 background trajectories are released, which experience no direct emission, but can interact with the "emission trajectories", representing mixing and dilution of the air parcels.

B. *Ozone-Chemistry*

For the calculation of aviation-induced climate cost functions, we consider additional NO_x emissions in the time-regions of interest. Aviation NO_x emissions influence ozone production and loss, and the partitioning of HO_x and hence influence methane depletion. From the detailed background chemistry in EMAC, we obtain the relevant production and loss rates. These are employed in the following tagging approach. The contribution of an emission e to the ozone production via, e.g., the reaction:

$$HO_2 + NO \rightarrow OH + NO_2 \qquad \text{(R1)}$$

is, according to [18]:

$$P_{O_3}^{e} = P_{O_3}^{b} \cdot \frac{1}{2}\left(\frac{HO_2^{e}}{HO_2^{b}} + \frac{NO^{e}}{NO^{b}}\right) \qquad (1)$$

where the superscript b indicates the background values and the superscript e indicates the respective values related to the emission at time-region R_i. PO_3 denotes the ozone production rate in [molecules/cm^3/s]. The reaction rate for loss terms of tagged species is determined in the same manner, e.g. for the reaction

$$NO_2 + O_3 \rightarrow NO + 2O_2, \qquad \text{(R2)}$$

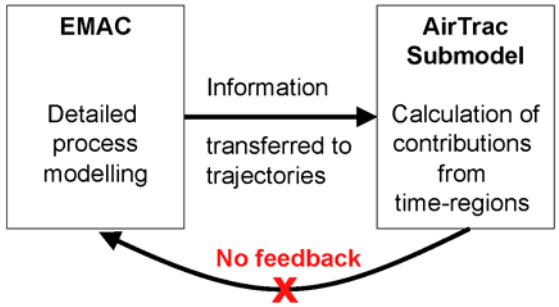

Figure 2. Schematic illustration of the transfer of information between the basemodel EMAC and the submodel AIRTRAC.

the loss term $L^e_{O_3}$ is

$$L^e_{O_3} = L^b_{O_3} \cdot \frac{1}{2}\left(\frac{NO^e_2}{NO^b_2} + \frac{O^e_3}{O^b_3}\right) \tag{2}$$

Note that the first term in brackets includes the depletion of background ozone by NO^e_2. Equations (1) and (2) only represent the contribution from an emission e to reactions (R1) and (R2). The following simplifications are introduced. We combine background species to families and calculate the contributions of time-region emissions according to the family concept, with the assumption that the emissions are small enough that the specific reaction rates are unchanged, i.e.:

$$\frac{P^b_{O_3}}{HO^b_2 \cdot NO^b} = \frac{P^b_{O_3} + P^e_{O_3}}{\left(HO^b_2 + HO^e_2\right)\cdot\left(NO^b + NO^e\right)} \tag{3}$$

Further, we regard the ozone production as primarily NO_x dependent. Whereas the ozone destruction is split into two parts driven by different chemical families: one based on NO_x the other one takes into account all other loss processes, yielding the following differential equation for ozone:

$$\frac{d}{dt}O^e_3 = \frac{P^b_{O_3}}{NO^b_x}NO^e_x - \frac{1}{2}D^b_{O_3,1}\left(\frac{NO^e_x}{NO^b_x} + \frac{O^e_3}{O^b_3}\right) - D^b_{O_3,2}\frac{O^e_3}{O^b_3} \tag{4}$$

This implicitly includes the assumption that the ratio of NO to NO_2 is equal in the background and the emitted NO_x. The emitted NO_x can be converted to HNO_3 which is eventually scavenged or can be reconverted to NO_2.

C. *Methane-Chemistry*

A similar approach is used for methane. We take into account the most relevant reactions regarding the concentration of OH and HO_2. The production of OH:

$$H_2O + O^1D \rightarrow 2OH \tag{R3}$$

$$HO_2 + O_3 \rightarrow OH + 2O_2 \tag{R4}$$

$$HO_2 + NO \rightarrow OH + NO_2 \tag{R5}$$

The loss of OH:

$$OH + O_3 \rightarrow HO_2 + O_2 \tag{R6}$$

$$OH + CO + O2 \rightarrow HO_2 + CO_2 \tag{R7}$$

$$OH + RH + O_2 \rightarrow RO_2 + H_2O \tag{R8}$$

$$OH + CH_4 \rightarrow CH_3O_2 + H_2O \tag{R9}$$

$$OH + HO_2 \rightarrow H_2O + O_2 \tag{R10}$$

The production HO_2 in addition to (R6) and (R7):

$$RO_2 + NO \rightarrow H_2O + R'CHO + NO_2 \tag{R11}$$

The loss of HO_2 in addition to (R4), (R5) and R(10):

$$RO_2 + HO_2 \rightarrow ROOH + O_2 \tag{R12}$$

$$HO_2 + HO_2 \rightarrow H_2O_2 + O_2 \tag{R13}$$

We are not considering aircraft contributions for H_2O, CO, RH and CH_4 for this approach, since their effects on OH can be considered to be small. We derive in analogy the production and loss terms for HO^e_2 and obtain a differential equation. The production and loss of OH^e, OH of the respective emission category, follows in analogy to eq. (1):

$$\begin{aligned} P^e_{OH} &= P^b_{R3}\frac{O^e_3}{O^b_3} + \frac{1}{2}P^b_{R4}\left(\frac{HO^e_2}{HO^b_2} + \frac{O^e_3}{O^b_3}\right) \\ &+ \frac{1}{2}P^b_{R5}\left(\frac{HO^e_2}{HO^b_2} + \frac{NO^e_x}{NO^b_x}\right) \end{aligned} \tag{5}$$

and

$$\begin{aligned} D^e_{OH} &= \frac{1}{2}D^b_{R6}\left(\frac{OH^e}{OH^b} + \frac{O^e_3}{O^b_3}\right) \\ &+ D^b_{R7}\frac{OH^e}{OH^b} + D^b_{R8}\frac{OH^e}{OH^b} + D^b_{R9}\frac{OH^e}{OH^b} \\ &+ \frac{1}{2}D^b_{R10}\left(\frac{OH^e}{OH^b} + \frac{HO^e_2}{HO^b_2}\right) \end{aligned} \tag{6}$$

In analogy we derive the production and loss terms for HO^e_2 and obtain differential equations for OH^e and HO^e_2, which can easily be solved:

$$\begin{aligned} \frac{d}{dt}OH^e &= P^e_{OH} - D^e_{OH} \\ &= A_0 + A_1\frac{HO^e_2}{HO^b_2} + A_2\frac{OH^e}{OH^b} \\ &= 0 \end{aligned} \tag{7}$$

$$\frac{d}{dt} HO_2^e = P_{HO_2}^e - D_{HO_2}^e$$
$$= B_0 + B_1 \frac{HO_2^e}{HO_2^b} + B2 \frac{OH^e}{OH^b} \quad (8)$$
$$= 0$$

$$OH^e = OH^b \frac{A_0 B_1 - A_1 B_0}{A_1 B_2 - A_2 B_1} \quad (9)$$

$$HO_2^e = HO_2^e \frac{A_2 B_0 - A_0 B_2}{A_1 B_2 - A_2 B_1} \quad (10)$$

$$A_0 = \left(P_{R3}^b + \frac{1}{2} P_{R4}^b - \frac{1}{2} D_{R6}^b \right) \frac{O_3^e}{O_3^b} + \frac{1}{2} P_{R5}^b \frac{NO_x^e}{NO_x^b} \quad (11)$$

$$A_1 = \frac{1}{2} \left(P_{R4}^b + P_{R5}^b - D_{R10}^b \right) \quad (12)$$

$$A_2 = -\frac{1}{2} D_{R6}^b - D_{R7}^b - D_{R8}^b - D_{R9}^b - \frac{1}{2} D_{R10}^b \quad (13)$$

$$B_0 = \frac{1}{2} \left(D_{R6}^b - P_{R4}^b \right) \frac{O_3^e}{O_3^b} + \left(P_{R11}^b - \frac{1}{2} P_{R5}^b \right) \frac{NO_x^e}{NO_x^b} \quad (14)$$

$$B_1 = -\frac{1}{2} P_{R4}^b - \frac{1}{2} P_{R5}^b - \frac{1}{2} D_{R10}^b - P_{R12}^b - \frac{1}{2} P_{R13}^b \quad (15)$$

$$B_2 = \frac{1}{2} D_{R6}^b + D_{R7}^b + \frac{1}{2} D_{R10}^b \quad (16)$$

The methane depletion caused by the contribution of aircraft emissions to the OH concentration is then

$$D_{CH_4}^e = D_{R9}^b \frac{OH^e}{OH^b} = D_{R9}^b \frac{A_0 B_1 - A_1 B_0}{A_1 B_2 - A_2 B_1} \quad (17)$$

D. Aviation-induced water vapor

Similarly to the NO_x emissions, also H_2O emissions from aviation are directly emitted on the Lagrangian trajectories at each time-region. The aviation-induced water vapor experiences the same loss processes through rain and snow formation as natural water vapor. The detailed background processes are derived from the CLOUD and CONVECT subroutines within EMAC, and the loss rates are then applied proportionally to the aviation water vapor. This facilitates an immediate analysis of aviation-induced water vapor, water vapor lifetime for emissions at different time-regions and for different transport pathways to different geographic regions and altitudes.

E. Aviation-induced cloudiness

Contrails form in the atmosphere, when the ambient air at flight levels is sufficiently cold and moist (Schmidt-Appleman criterion, SAC) [20]. Once formed, contrails may persist if the air is supersaturated relative to ice. When persistent, contrails may spread into contrail cirrus clouds and last for several hours. We determine the atmospheric ability to form persistent contrails, i.e. the potential contrail coverage, instantaneously within the climate model at each time step similar to [21]. The potential contrail coverage, b_{co} is:

$$b_{co+cc} = \begin{cases} \frac{r - r_{co}}{r_{sat} - r_{ci}} - b_{ci}(1 - b_{ci}) : & r_{co} \le r < r_* \\ 1 & : r > r_* \end{cases}, \quad (18)$$

$$b_{co} = b_{co+ci} - b_{ci} \quad (19)$$

with b_{ci}:

$$b_{ci} = 1 - \sqrt{\frac{r - r_{ci}}{r_{sat} - r_{ci}}} \quad (20)$$

The critical relative humidity for contrail formation, r_{co} may be calculated via

$$\frac{r_{co}}{r_{ci}} = r_{SAC} / (a \cdot r_{nuc}), \quad (21)$$

with r_{SAC} being the relative humidity over ice at which the Schmidt-Appleman-Criterion is fulfilled during the mixing of aircraft exhaust gases and ambient air, r_{nuc} is the homogeneous freezing threshold. As contrails often form prior to the formation of natural cirrus a is chosen to be *0.9*, similarly to [21].

The potential contrail coverage is transferred to the Lagrangian trajectories. Then the actual contrail coverage is calculated depending on whether air traffic is actually taking place in the respective grid box.

$$b_{new} = \frac{W_0 \cdot L}{A} \quad (22)$$

$$L = D \cdot b_{co} \quad (23)$$

A fixed initial contrail width W_0 of 200 m is assumed. The length of each contrail indicates the portion of the flight distance per model grid box and time step allowing for contrail formation according to the potential contrail coverage b_{co}. A is the area of the model grid box.

The spreading of contrails is parameterized as in [22], in dependency of a vertical wind shear vector, the contrail length L and the vertical thickness H of the contrail, which is here assumed to be 200 m for a 15 minutes old contrail [23]:

$$\left(\frac{db}{dt}\right)_{spr} = c \cdot \sqrt{\left(\frac{du}{dz}\right)^2 + \left(\frac{dv}{dz}\right)^2} \cdot \frac{H \cdot L}{A} \tag{24}$$

The total contrail coverage b of new and aged, i.e. spread, contrails is then given by:

$$\frac{db}{dt} = \left(\frac{db}{dt}\right)_{new} + \left(\frac{db}{dt}\right)_{spr} \tag{25}$$

Similar to [24] we assume, that the contrail ice water mixing ratio m depends on the condensation rate in the contrail covered part of the grid box c_{co},

$$\left(\frac{dm}{dt}\right)_{new} = c_{co} \ , \tag{26}$$

which is defined analogously to the condensation rate for natural clouds:

$$c_{co} = R(q) - \frac{dq_s}{dt} \ . \tag{27}$$

If the contrail persists, contrail ice water is transferred to the next time step and can then undergo sedimentation, which is parameterized following [25], similarly to the sedimentation of cirrus particles in ECHAM5.

$$\left(\frac{dm}{dt}\right)_{sed} = \frac{1}{\rho} \cdot \frac{dF}{dz}, F = v \cdot m \cdot \rho, v = \alpha \cdot (\rho \cdot m)^{\beta} \tag{28}$$

where F is the flux of ice particles (in terms of mixing ratio), v is the fall velocity, $\alpha=3.29$ and $\beta=0.16$. Furthermore contrail ice water increases or decreases if potential contrail coverage changes, which can be understood as growth and sublimation of ice particles, related to changes in the humidity.

$$\left(\frac{dm}{dt}\right)_{subl/grow} = \frac{\frac{b_{co}^{t+1} - b_{co}^{t-1}}{b_{co}^{t-1}}}{dt} \cdot m^{t-1} = \frac{d \ln b_{co}}{dt} \cdot m^{t-1} \tag{29}$$

The overall contrail ice water mixing ratio is then defined by:

$$\frac{dm}{dt} = \left(\frac{dm}{dt}\right)_{new} + \left(\frac{dm}{dt}\right)_{sed} + \left(\frac{dm}{dt}\right)_{subl/grow} \tag{30}$$

F. Radiative forcing

The instantaneous radiative forcing is calculated online in EMAC for both ozone and contrails, for every time-region separately. The distributions of the radiatively active species are therefore transferred from Lagrangian to grid space. However, not the instantaneous, but the stratosphere adjusted radiative forcing is considered to be the most significant indicator for climate impact. But the process of stratospheric adjustment would require that the timescale of the perturbation is long enough to enable stratospheric temperatures to adjust. This is not the case in the present study, as we are looking at pulse emissions and the related decline of the perturbation, which is in case of the ozone a time period of a few months.

The radiative forcing of contrails depends on the fractional coverage, the optical properties of contrails, the altitude of contrail, and the change of the system albedo. With respect to contrail radiative forcing, the difference between the instantaneous and the adjusted radiative forcing is negligible [26], therefore we use the instantaneous radiative forcing for the calculation of the contrail climate cost function.

The water vapor radiative forcing is based on results from [13], relating a mean radiative forcing to a global change in water vapor mass of 2.5×10^{-13} mW/m^2/kg(H_2O). This assumes that the most important effect is the lifetime of the water vapor perturbation, which is explicitly simulated leading to a change in water vapor mass.

The methane radiative forcing is calculated according to a well-established non-linear relation between an atmospheric concentration change and the radiative forcing [27].

The stratosphere adjusted radiative forcing of ozone differs significantly from the instantaneous ozone radiative forcing [e.g. 28]. The difference between adjusted and instantaneous forcing was found to depend on the vertical distribution of the ozone perturbation.

We parameterize the adjusted ozone radiative forcing from the instantaneous radiative forcing, based on simulations with idealized ozone perturbations at different altitudes which were taken from [15]. These experiments show a distinct difference between the instantaneous and the adjusted ozone radiative forcing, even a change of sign in the relation of instantaneous and adjusted forcing for different vertical ozone distributions. For tropospheric perturbations, the instantaneous radiative forcing is larger than the adjusted radiative forcing, as the adjustment of stratospheric temperatures leads to stratospheric cooling, which implies a negative feedback to the radiative flux at the tropopause. Whereas, for ozone perturbations in the lower stratosphere, the adjusted radiative forcing is larger than the instantaneous forcing, as the ozone perturbation leads to a dipole pattern in the adjusted temperatures, an increase in temperature in the lower stratosphere and a decrease in

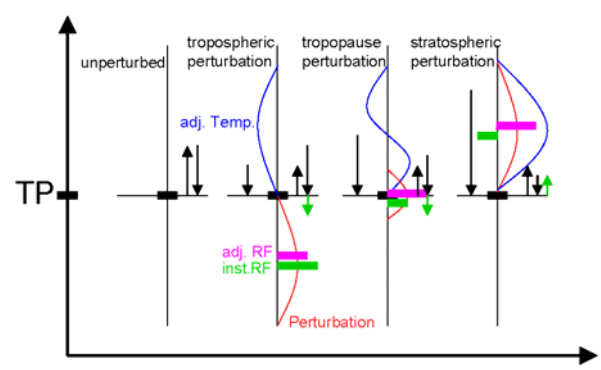

Figure 3. Schematic representation of the relation between instantaneous (green) and adjusted (pink) ozone radiative forcing for different perturbation altitudes. The perturbation distribution is given in red, the stratospheric temperature adjustment is shown in blue. The arrows to the right of the vertical lines indicate the total up and downward radiative fluxes, the arrows to the left from the vertical lines give the downward flux related to the stratospheric temperature adjustment for each situation.

temperatures above. This is schematically shown in Fig.3.

The differences between adjusted and instantaneous ozone radiative forcing vary over the seasonal cycle, and the seasonal variation depends on the perturbation altitude. The ratio of the maximum adjusted to the maximum instantaneous radiative forcing is used to derive the adjusted radiative forcing. From the above mentioned experiments and earlier simulations performed by [29] we derive altitude (p) and time (t) dependent factors to scale the instantaneous radiative forcing:

$$adjRF = f_1(p) \cdot f_2(t) \cdot instRF \,, \qquad (31)$$

where f_1 and f_2 are functions, depending on the time-region of the emission, i.e. the time of the year *t* and pressure *p*, when and where the emissions are released. The seasonal cycle can be described by a sinus function:

$$f_1(t) = f_1^{mean}\left[\sin\left(2\pi\frac{t-7.5}{12}+\frac{\pi}{2}\right)-1\right] \qquad (32)$$

with $f_1^{mean}=0.08$, the amplitude of the deviation from the annual mean and the time of the year *t* in months.

The altitudinal dependency of the ratio of the instantaneous to the adjusted radiative forcing is characterized by the stratospheric temperature adjustment and the location of the perturbation relative to the tropopause. This relation is schematically shown in Fig. 3. With increasing height of the perturbation, the instantaneous radiative forcing (green) turns from positive to negative, because of the flux changes at the tropopause (arrows). The stratosphere is cooled for tropospheric perturbations, whereas stratospheric perturbations result in a warming at the perturbation altitude and a cooling above. The adjusted temperatures (blue) turn from negative to positive, with a dipole structure in between. The function f_2 describing the altitudinal dependency of the relation between instantaneous and adjusted radiative forcing is derived from idealized experiments (see Fig. 4). The fit resembles the overall structure, but as the database is limited, it includes some uncertainty.

$$f_2 = C - A\frac{E_p - D}{B(E_p - D)^2 + 1} \qquad (33)$$

with *A=1.1, B=2.0, C=1.05, D=3.4, E=1/60*.

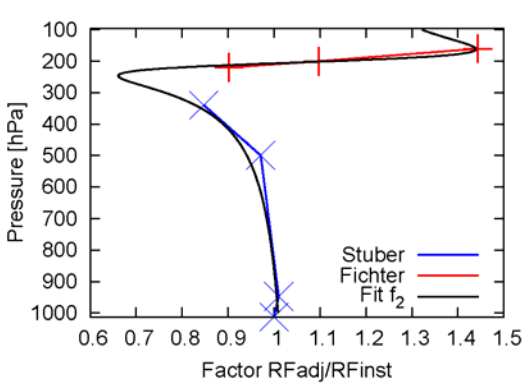

Figure 4. Altitudinal dependency of the relation between instantaneous and adjusted radiative forcing, based on idealized experiments from [29] and [15].

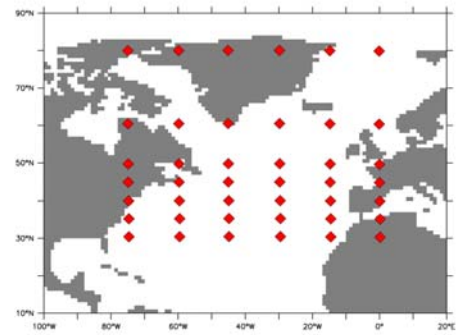

Figure 5. Geographical distribution of time-regions in the North Atlantic region.

III. Results

For every typical weather situation which was identified in the North Atlantic region climate cost functions are calculated for a number of time-regions. Aviation emissions are released at 7 latitudes between 30°N and 80°N, at 6 longitudes between 75°W and 0°W, at four pressure levels between 200 and 400 hPa, and at 3 times between 6:00 and 18:00. The geographical distribution of time-regions is shown in Fig. 5. In total, climate cost functions for ~500 time-regions are determined per weather situation.

In the following we will present first results of chemical perturbations, contrails and radiative forcings for the weather situation "strong zonal jet" [16]. Fig. 6 shows the temporal development of total global ozone and global ozone net radiative forcing in addition to the averaged horizontal and vertical distribution for two different emission locations at 200 hPa, 30°N, 60° W or 200 hPa, 30°N, 75°W. Although the two emission regions are nearby, the overall effect on ozone and ozone radiative forcing can be very different. This is mainly due to diverging transport pathways, to regions where the emissions experience different production and loss processes. The emissions which were released at 75°W are primarily transported to the mid and lower troposphere and towards the tropics. The ozone production efficiency is very high there, thus the trajectories with the NO_x emissions experience high ozone production rates. Whereas the emissions released at 60°W stay at mid latitudes and close to the tropopause, experience smaller ozone production. In principle, ozone residing in the tropics and close to the tropopause causes a larger specific radiative impact than ozone at high latitudes and lower tropospheric levels.

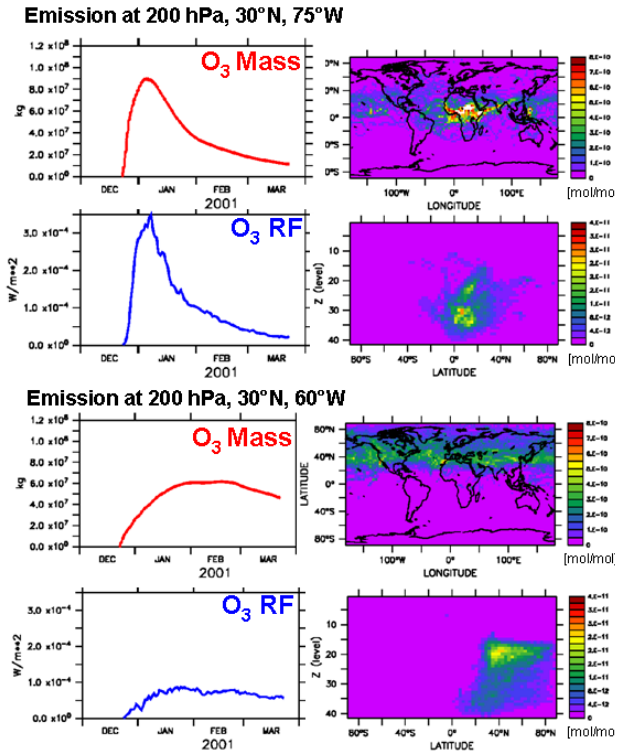

Figure 6. Temporal development of the total global ozone perturbation, the related instantaneous ozone radiative forcing, the averaged vertical and horizontal distribution of the ozone perturbation for two different emssion locations at 200 hPa, 30°N, 75°W and 200 hPa, 30°N, 60°W.

Fig. 7 shows the temporal development of contrail coverage and their optical properties and instantaneous radiative forcing for two different, arbitrarily chosen emission locations. Large differences in their optical properties and net radiative forcing of up to two orders of magnitude can be observed, which are caused by differing ambient conditions during formation and aging. In this case the contrails imply largely a positive net radiative forcing, but for very small ice water contents and high solar zenith angles even negative net radiative forcing can be observed. Considerable differences with respect to the lifetimes of contrails can be seen, from dissolving immediately after formation up to ~24 hours.

Fig. 8 shows exemplarily the climate cost functions of H_2O and CH_4 for the chosen weather situation as functions of latitude and altitude at 30°W. Here we show the adjusted radiative forcing, which serves as the basis for other possible metrics like global warming potential or global temperature potential. The water vapor climate cost function increases with height, and is particularly high for emissions released in the stratosphere. Because of the lack of major loss processes, the lifetimes of water vapor are much longer for stratospheric emissions. The CH_4 climate cost function in contrast increases (in absolute values) towards the tropics and from the tropopause towards mid-tropospheric altitudes. Because of the high water vapor concentrations in the tropical mid to lower troposphere and strong solar insolation, NO_x emissions cause efficient production of OH which in turn results in strong CH_4 depletion. The O_3 radiative forcing (not shown) increases with

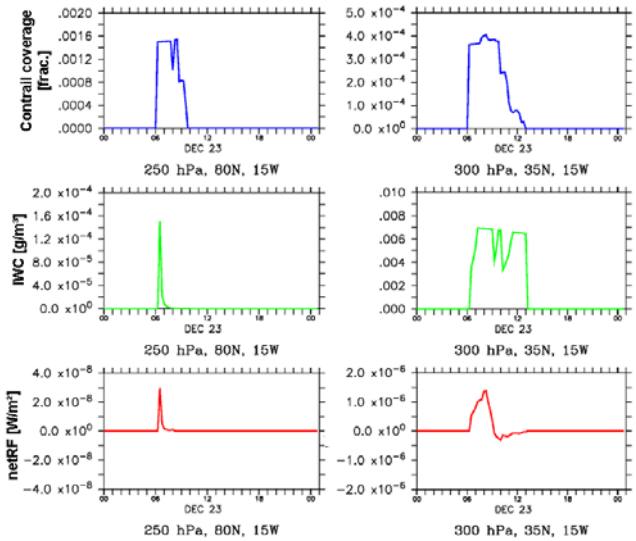

Figure 7. Temporal development of fractional contrail coverage, ice water content and the related contrail radiative forcing for two different emission locations at 250 hPa, 80°N, 15°W and 300 hPa, 35°N, 15°W.

altitude, thus the O_3 and the CH_4 radiative forcing are anti-correlated.

Fig. 9 shows exemplarily the climate cost function for contrails and ozone as functions of longitude and latitude at an emission altitude of 200 hPa. The contrail radiative forcing shows strong local variations. Both positive and negative

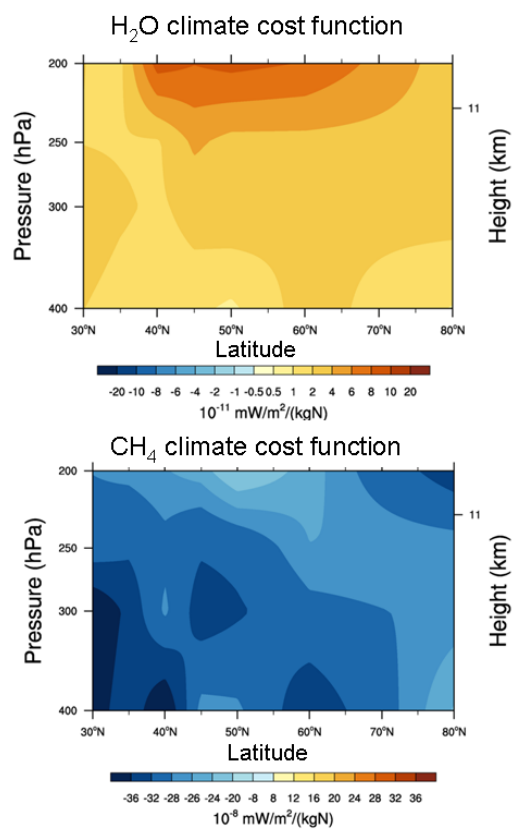

Figure 8. H_2O (top) and CH_4 (bottom) climate cost function in terms of adjusted net radiative forcing for weather pattern "strong zonal jet" as a function of altitude (pressure) and latitude at 30°W.

radiative forcings can be observed and large areas with no contrail formation at all. This is due to the general distribution and extent of ambient conditions, suitable for contrail formation, i.e. ice super saturated regions [30]. The climate

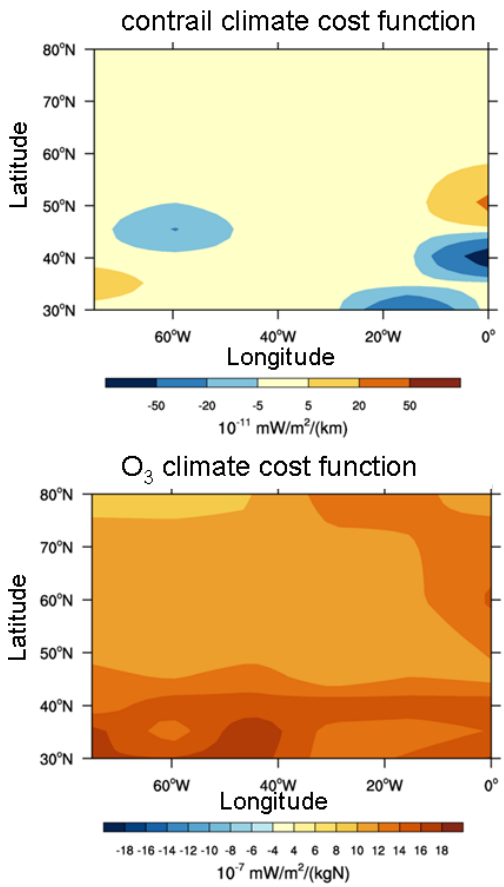

Figure 9. Contrail (top) and O_3 (bottom) climate cost function in terms of adjusted net radiative forcing for weather pattern "strong zonal jet" as a function of latitude and longitude at 200 hPa.

cost function of ozone increases strongly towards the tropics because of the high ozone production efficiency in the tropics. At high northern latitudes ozone climate cost functions have small to moderate values because of missing sun light in winter time and therefore reduced photo chemistry, unless emissions are transported southwards as it is the case between 0° and 20°W.

IV. Conclusions and Outlook

The development of the new submodel AIRTRAC for the ECHAM5/MESSy Atmospheric Chemistry Model has been completed. AIRTRAC is a very flexible tool and facilitates the calculation of weather dependent climate cost functions for various emission locations, altitudes and times within one simulation. The following species are considered: O_3, CH_4, primary mode ozone, H_2O, contrails and CO_2. These climate cost functions serve as a basis for weather dependent climate optimized flight trajectory planning. First results of climate cost functions calculated by EMAC/ATTILA/AIRTRAC were shown and discussed. We have performed a multitude of sensitivity checks and comparison to other studies, to make sure that the model gives reasonable results with respect to chemical perturbations, contrails, contrail optical properties and radiative forcing.

It was found, that the climate cost functions show a large spatial variability. Features of the weather pattern e.g. predominant transport pathways, precipitation areas, tropopause height, etc. and their impact on chemical production efficiency, scavenging, chemical lifetimes, etc. can be identified within of the climate cost functions. This indicates a large mitigation potential. However, the optimization of flight trajectories is not trivial because of anti-correlations between different species, e.g. O_3 and CH_4.

In future work, we will further investigate the interrelationship of the climate cost functions and their correlation to typical weather patterns. The cost functions will be employed for optimizing air traffic flight trajectories with respect to minimum climate impact [31, 32, 33]. First results will be shown at the Tenth USA/Europe Air Traffic Management Research and Development Seminar (ATM2013) and can be found in [34].

Acknowledgment

This work was performed within the EU FP7 Project REACT4C (www.react4c.eu). The simulations were run on the supercomputer of the Deutsches-Klima-Rechenzentrum (DKRZ) in Hamburg, Germany.

References

[1] Sausen, R., K. Gierens, M. Ponater, U. Schumann, 1998: A diagnostic study of the global distribution of contrails. Part1: Present day climate, Theor. Appl. Climatol., 61, 3, 127-141.

[2] Grewe, V., M. Dameris, C. Fichter, D. Lee, 2002: Impact of aircraft NO_x emissions. Part 2: Effects of lowering the flight altitude, Meteorol. Zeitschr., 11, 3, 197-205.

[3] Fichter, C., S. Marquart, S. Sausen, D. Lee, 2005: The impact of cruise altitude on contrails and related radiative forcing. Meteorol. Zeitschrift, 14, 4, 563-572 .

[4] Gauss, M., I. Isaksen, D. Lee, O. Sρvde, 2006: Impact of aircraft NO_x emissions on the atmosphere – Tradeoffs to reduce the impact, Atmos. Chem. Phys., 6, 1529-1548.

[5] Köhler, M., G. Rädel, O. Dessens, K. Shine, H. Rogers, O. Wild, J. Pyle, 2008: Impact of perturbations to nitrogen oxide emissions from global aviation, J. Geophys. Res. 113, D11.

[6] Rädel, G., K. Shine, 2008: Radiative forcing by persistent contrails and its dependence on cruise altitudes, J. Gephys. Res. 113.

[7] Frömming, C., M. Ponater, U. Burkhardt, A. Stenke, S. Pechtl, R. Sausen, 2012: Sensitivity of contrail coverage and contrail radiative forcing to selected key parameters, Atm. Environ. 45, 1483-1490.

[8] Williams, V., R. Noland, R. Toumi, 2002: Reducing the climate change impacts of aviation by restricting cruise altitudes, Transport. Res., D7, 6, 451-464.

[9] Mannstein, H., P. Spichtinger, K. Gierens, 2005: A note on how to avoid contrail cirrus, Transport. Res., D10, 5, 421-426.

[10] Gauss, M., I. Isaksen, S. Wong, W. Wang, 2003: Impact of H_2O emissions from cryoplanes and kerosene aircraft on the atmosphere, J. Geophys. Res., 108, 10.

[11] Wilcox, L.J., K.P. Shine, B.J. Hoskins, 2012: Radiative forcing due to aviation water vapour emissions. Atmospheric Environment, 6, 1-13.

[12] Stordal, F., M. Gauss, G. Myhre, E. Mancini, D. Hauglustaine, M. Köhler, T. Berntsen, E. Stordal, D. Iachetti, G. Pitari, I. Isaksen, 2006:

Tradeoffs in climate effects through aircraft routing: forcing due to radiatively actove gases, Atmosph. Chem. Phys. Discuss., 6, 10733-10771.

[13] Frömming, C., M. Ponater, K. Dahlmann, V. Grewe, D. S. Lee, R. Sausen, 2012: Aviation-induced radiative forcing and surface temperature change in dependency of the emission altitude, J. Geophys. Res., 117, D19104, doi:10.1029/2012JD018204.

[14] Grewe, V., A. Stenke, 2008: AirClim: An efficient tool for climate evaluation of aircraft technology, Atmosph. Chem. Phys., 8, 4621-4639.

[15] Fichter, C., 2009: Climate impact of air traffic emissions in dependency of the emission location and altitude, PhD Thesis, DLR-Forschungsbericht 2009-22, ISSN 1434-8454.

[16] Irvine, E.A., B.J. Hoskins, K. P. Shine, R. W. Lunnon, C. Fromming, 2011: Characterising North Atlantic weather patterns for climate-optimal aircraft routing, Meteorol. Appl., doi:10.1002/met1291, in press.

[17] Jöckel, P., A. Kerkweg, A. Pozzer, R. Sander, H. Tost, H. Riede, A. Baumgaertner, S. Gromov, B. Kern, 2010: Development cycle 2 of the Modular Earth Submodel System (MESSy2), Geoscientific Model Development, 3, 717–752, doi: 10.5194/gmd-3-717-2010.

[18] Reithmeier , C., R. Sausen, 2002: ATTILA: Atmospheric tracer transport in a Lagrangian model, Tellus B, 54, 3, 278-299.

[19] Grewe, V., E. Tsati, P. Hoor, 2010: On the attribution of contributions of atmospheric trace gases to emissions in atmospheric model applications, Geosci. Model Dev., 3, 487-499.

[20] Schumann, U., 1996: On conditions for contrail formation from aircraft exhausts, Meteorol. Zeitschr. 5, 4-23.

[21] Burkhardt, U., B., Kärcher, M. Ponater, K. Gierens, A. Gettleman, 2008: Contrail cirrus supporting areas in model and observations, GEophys. Res. Lett., 35.

[22] Burkhardt, U., B. Kärcher, 2009: Process-based simulation of contrail cirrus in a global climate model, J. Geophys. Res. 114, D16.

[23] Freudenthaler, V., F. Homburg, and H. Jäger (1995), Contrail observations by ground-based scanning Lidar: Cross-sectional growth, Geophys. Res. Lett., 22, 3501– 3504.

[24] Ponater, M., S. Marquart, R. Sausen, 2002: Contrails in a comprehensive global climate model: Parameterization and radiative forcing results, J. Geophys. Res., 107, 13, 941-960.

[25] Heymsfield, A.J., L.J. Donner, 1990: A scheme for parameterizing ice cloud water content in general circulation models. J. Atmos. Sci., 47, 1865–1877.

[26] Marquart, S., 2003: Klimawirkung von Kondensstreifen: Untersuchungen mit einem globalen atmosphärischen Zirkulationsmodell, PhD Thesis, DLR-Forschungsbericht 2003-16.

[27] Ramaswamy, V., et al., 2001: Radiative forcing of climate change. In: Climate Change 2001: The Scientifi c Basis. Contribution of Working Group I to the Third Assessment Report of the Intergovernmental Panel on Climate Change [Houghton, J.T., et al. (eds.)]. Cambridge University Press, Cambridge, United Kingdom and New York, NY, USA, pp. 349–416.

[28] Haywood, J.M., M.D. Schwarzkopf, V. Ramaswamy, 1998:, Estimates of radiative forcing due to modeled increases in tropospheric ozone, J. Geophys. Res., 103(D14), 16999–17007, doi:10.1029/98JD01348.

[29] Stuber, N., 2003: Ursachen der Variabilität des Klimasensitivitäts-parameters für räumlich inhomogene Ozonstörungen, PhD Thesis, DLR-Forschungsbericht 2003-03.

[30] Gierens, K., P. Spichtinger, 2000: On the size distribution of ice-supersaturated regions in the upper troposphere and the lower stratosphere. – Ann. Geophysicae 18, 499–504.

[31] B. Sridhar, N.Y. Chen, and H.K. Ng, "Energy Efficient Concepts for Reducing the Environmental Impact of Aviation", Tenth USA/Europe Air Traffic Management Research and Development Seminar (ATM2013).

[32] H. Yamashita, V. Grewe, P. Jöckel, Climate assessment of routing strategies, Air Traffic Management Research and Development Seminar (ATM2013).

[33] S. Matthes, U. Schumann, V. Grewe, C. Frömming, K. Dahlmann, A. Koch, H. Mannstein, Climate Optimized Air Transport, 727-746, Ed. U. Schumann, ISBN 978-3-642-30182-7, ISBN 978-3-642-30183-4 (eBook), DOI 10.1007/978-3-642-30183-4, Springer Heidelberg New York Dordrecht London, 2012.

[34] V. Grewe, C. Frömming, S. Matthes, S. Brinkop, M. Ponater, S. Dietmüller, P. Jöckel, H. Garny, E. Tsati, O.A. Søvde, J. Fuglestvedt, G. Myhre, K.P. Shine, E. Irvine, T. Champougny, P. Hullah, 2013: Aircraft routing with minimal climate impact: The REACT4C cost function modelling approach (in preparation for Geosci. Model Dev.).

AUTHOR BIOGRAPHY

Dr. Christine Frömming works as a postdoctoral scientist at the German Aerospace Center (DLR), Institute for Atmospheric Physics. She received her diploma in physical geography from the Ludwig-Maximilians-University Munich, Germany and her PhD in environmental and geographical sciences from the Manchester Metropolitan University, UK in 2009. Her research interests include the altitude and location dependency of aviation climate impacts and weather dependent climate optimized flight routing.

Dr. Volker Grewe received his Diploma in mathematics from the University Augsburg, Germany, and his PhD in meteorology from the Ludwig-Maximilians-University Munich, Germany. He has been working as a scientist in the field of climate-chemistry interactions with focus on traffic and air traffic effects upon the atmosphere since 1992 at the DLR-Institute for Atmospheric Physics. He also worked at NASA-GISS in New York 1999-2000 and was a visiting scientist at NCAR (Boulder, Colorado) NASA-Ames, NASA-GISS and CICERO (Oslo, Norway). He is topical editor of the journal Geoscientific Model Development.

Dr. Patrick Jöckel received his diploma in physics from the Technische Universität Darmstadt, Germany and his PhD in natural and mathematical sciences from the University of Heidelberg, Germany. He coordinates the multi-institutional development and evaluation of the Modular Earth Submodel System (MESSy). In 2005 he received the Heinz Billing Award for the Advancement of Scientific Computation. He is an editor of the journal Atmospheric Chemistry and Physics, and Geoscientific Model Development. He worked at the Max-Planck-Institute of Chemistry in Mainz, Germany for many years. Since 2009 he works at the DLR-Institute for Atmospheric Physics.

Dr. Sabine Brinkop studied meteorology and received her PhD from the University of Hamburg, Germany in 1992. Over the last 25 years, she has been working as a scientist in several climate research groups (Meteorological Institute, University of Hamburg; Ludwig-Maximilians-University Munich; DLR-Institute for Atmospheric Physics) with a focus on model development, especially convection and Lagrangian transport within climate-chemistry models.

Dr. Simone Dietmüller received her PhD in meteorology at the Ludwig-Maximilians-University Munich, Germany in 2011. At the moment she is working as scientist at the German Aerospace Center (DLR), Institute for Atmospheric Physics. Her current research interests include climate forcings, climate feedbacks and climate sensitivity.

Dr. Hella Garny works as a postdoctoral scientist at the DLR, Institute for Atmospheric Physics in the field of atmospheric dynamics. She received her PhD in meteorology from the Ludwig-Maximilians-University Munich, Germany in 2010. She was a visiting scientist at NIWA Lauder, New Zealand in 2007 and 2009. From 2011 to 2012 she worked at NCAR Atmospheric Chemistry Divison in Boulder, Colorado.

Dr. Michael Ponater earned his PhD in meteorology in 1985 at the University of Cologne, Germany. He has been working as a scientist in several climate research groups (Meteorological Institute, University of Hamburg; Max-Planck-Institute for Meteorology, Hamburg; DLR-Institute for Atmospheric Physics) over the last 25 years, specializing on topics related to climate effects caused by aviation and other transport systems.

Eleni Tsati received her diploma in physics from the University of Patras, Greece in 2006. She is a PhD student at Ludwig-Maximilians-University Munich, Germany. She works in the field of tropospheric chemistry and physics and the impact of anthropogenic emissions on the atmosphere at the DLR-Institute of Atmospheric Physics since 2009.

Dr. Sigrun Matthes received her diploma in physics from the Technical University Munich, Germany in 1997, and her PhD in meteorology from Ludwig-Maximilians-University Munich, Germany in 2003. She has been working as a scientist at the DLR-Institute of Atmospheric Physics since 1998 in the field of atmospheric modelling. She is coordinator of the EU FP7 project REACT4C, and chair of ECATS IASBL on sustainable aviation.